

Two pathways of how remote SST anomalies drive the interannual variability of autumnal haze days in the Beijing–Tianjin–Hebei region, China

Jing Wang¹, Zhiwei Zhu^{1*}, Li Qi¹, Qiaohua Zhao¹, Jinhai He¹, and Julian X. L. Wang²

¹Key Laboratory of Meteorological Disaster, Ministry of Education (KLME)/Joint International Research Laboratory of Climate and Environment Change (ILCEC)/Collaborative Innovation Center on Forecast and Evaluation of Meteorological Disasters (CIC-FEMD), Nanjing University of Information Science and Technology, Nanjing, China

²Air Resources Laboratory, National Oceanic and Atmospheric Administration, College Park, MD, USA

* Correspondence to: Zhiwei Zhu (zwz@nuist.edu.cn)

Abstract. Analogous to the circumstances in wintertime, the increasing severity of autumnal haze pollution over the Beijing–Tianjin–Hebei (BTH) region may also lead to impairment of the socioeconomic development and human health in this region. Despite manmade aerosol emissions, the interannual variability of autumnal (September–October–November) haze days (AHD) in the BTH region (AHD_{BTH}) is apparently tied to the global and regional meteorological anomalies. The present study suggests that an above-normal AHD_{BTH} is closely associated with the simultaneous sea surface temperature (SST) warming in two regions [over the North Atlantic subtropical sector (R1) and over the western North Pacific sector (R2)]. When the autumnal SST warming in R1 and R2 are both significant, the likelihood of a higher AHD_{BTH} is greatly enhanced. Observational and simulation evidence demonstrated how remote SST anomalies over R1 and R2 influence variation of AHD_{BTH} via two different pathways. Firstly, SST warming in R1 can induce a downstream mid-latitude Rossby wave train, leading to a barotropic high-pressure and subsidence anomaly over the BTH region. Secondly, SST warming in R2 can also result in air subsidence over the BTH region through an anomalous local meridional cell. Through these two distinct pathways, localized meteorological circumstances conducive to a higher AHD_{BTH} (i.e., repressed planetary boundary layer, weak southerly airflow, and warm and moist conditions) can be established.

1 Introduction

Aerosol particles (APs) are ubiquitous in the ambient air. Through aerosol-induced thermal forcing, APs can exert profound impacts on regional and large-scale circulation (e.g., Chung et al., 2002; Lau and Kim, 2006; Lau et al., 2006; Liu et al., 2009; Li et al., 2016; Wu et al., 2016), as well as global warming (e.g., Charlson et al., 1992; Tett et al., 1999; Zhang et al., 2016). Notably, due to the property of light extinction related to high concentrations of APs, especially fine particulate matter [i.e., particulate matter (PM) with an aerodynamic diameter of 2.5 μm or less ($PM_{2.5}$)] (Guo et al., 2014; Wang et al., 2014; Li et al., 2017; Seo et al., 2017; Chen et al., 2018; Luan et al., 2018), severe haze weather with low visibility can readily occur (Chen et al., 2012; Li et al., 2016; Ding et al., 2017; Seo et al., 2017; Chen et al., 2018).

In recent decades, observational evidence suggests that China has become one of the most severe AP-loading regions in the world (Tao et al., 2016; Li et al., 2016), arguably because of the nationwide rapid industrialization and urbanization (Xu et al., 2015; Zhang et al., 2016). High concentrations of APs can lead to the formation of severe haze weather via complicated interactions (Wang et al., 2014). Haze weather is not only harmful to the human respiratory and cardiovascular systems (Pope III and Dockery, 2006; Tie et al., 2009; Chen et al., 2013; Xu et al., 2013), but also influences vehicular traffic and crop yields (Chameides et al., 1999; Wu et al., 2005). As a result, haze pollution has received considerable attention from the government and the public. Unfortunately, on the one hand, overwhelming industrialization leads to more severe haze contamination over the Beijing–Tianjin–Hebei (BTH) region (Yin and Wang, 2016); whilst on the

49 other hand, the trumpet-shaped topography (Fig. 1) of the region is unfavorable for the dissipation
50 of air pollution, thus making the BTH region home to some of the worst haze weather in China.
51 Since the BTH region is the most economically developed region in North China and is at the
52 heart of Chinese politics and culture, severe haze pollution in this region has become a critical
53 issue (e.g., Mu and Zhang, 2014; Wang, 2018), especially since the occurrence of the
54 unprecedented severe haze event in North China in January 2013 (Wang et al., 2014; Zhang et al.,
55 2014; Mu and Zhang, 2014; Tao et al., 2014; Zhang et al., 2015).

56 To date, numerous efforts have been made to explore the causes of wintertime haze pollution over
57 the BTH region and its surroundings, and these previous studies roughly fall into three categories
58 based on the climatological perspective. The first category reported that the joint effects of the
59 emissions of various sources of APs (e.g., Cao et al., 2007; Guo et al., 2011; Zhu et al., 2016) and
60 climate anomalies (e.g., Chen and Wang, 2015; Wang and Chen, 2016; Yin and Wang, 2016; Cai et
61 al., 2017; Wang, 2018) may have brought about the increasing severity of haze pollution over
62 China in recent decades. The second category of studies, meanwhile, underlines the causality of
63 the variation in winter haze days in eastern and northern China from the perspective of climate
64 anomalies (e.g., Li et al., 2016; Yin and Wang, 2016; Pei et al., 2018). For instance, it is suggested
65 that a weakened East Asian winter monsoon (EAWM) system could lead to the above-normal
66 numbers of winter haze days (e.g., Niu et al., 2010; Li et al., 2016; Yin and Wang, 2016).
67 Meanwhile, the variability of EAWM has been shown to be significantly tied to the East Atlantic–
68 West Russia pattern and Eurasian pattern (Zhang et al., 2016; Yin et al., 2017). The third category
69 focuses on the external forcings associated with the variability of winter haze days. These forcings
70 include the sea surface temperature (SST) (e.g., Gao and Li, 2015; Wang et al., 2015), Arctic sea
71 ice (e.g., Wang et al., 2015; Zou et al., 2017), Eurasian snowpack (e.g., Yin et al., 2017), and the
72 thermal conditions on the Tibetan Plateau (e.g., Xu et al., 2016). However, most of these previous
73 works have focused on wintertime, with little attention having been paid to other seasons.

74 Autumn is a transitional season from the wet and hot summer to the dry and cold winter.
75 Climatologically, the weather in autumn over the BTH region is quite pleasant, with favorable
76 temperatures and light winds. Outdoor activities and tourism are therefore prevailing in the
77 autumn season. However, autumn is also a season in which haze weather frequently occurs in
78 the BTH region (Chen and Wang, 2015). The number of autumnal haze days (AHDs) has
79 increased remarkably in recent years. Such an increase in the number of haze days is a potential
80 threat to tourism economics in this region. Therefore, research into the causes of the interannual
81 variation in AHDs in the BTH region (AHD_{BTH}) is imperative. Such work not only provides
82 scientific support to the year-to-year scheduling of anthropogenic emissions for dealing with
83 autumnal haze pollution, but also helps the government with facilitating the arrangement of
84 tourism economics. However, compared to the myriad studies on wintertime haze pollution,
85 autumn haze pollution over the BTH region has attracted far less attention, with only a few case
86 studies on atmospheric circulation having been reported (Yang et al., 2015; Gao and Chen, 2017;
87 Wang et al., 2018). It was this knowledge gap that motivated us to revisit the variability of
88 AHD_{BTH} . Considering that the SST acts as a crucial driver of large-scale climate variability (e.g.,
89 Wang et al., 2009; Zhu et al., 2014; He and Zhu, 2015; Xiao et al., 2015; Zhu and Li, 2017; Zhu,
90 2018), we aimed to figure out the underlying air–sea interaction mechanisms for the interannual
91 AHD_{BTH} variability in the present study.

92 The remainder of this paper is organized as follows. Section 2 introduces the data, model and
93 methodology. Section 3 presents the atmospheric anomalies associated with AHD_{BTH} . Section 4
94 addresses the mechanisms of how remote SST anomalies (SSTAs) drive the interannual variations
95 of AHD_{BTH} . Conclusions and further discussion are provided in the final section.

96 **2 Data, model and methodology**

97

98 **2.1 Data**

99 The data used in this study are as follows: (1) monthly mean planetary boundary layer height
100 (PBLH), with a $1^\circ \times 1^\circ$ horizontal resolution, from the European Centre for Medium-Range
101 Weather Forecasts Interim Reanalysis (ERA-Interim) (Dee et al., 2011); (2) monthly mean
102 atmospheric data with a $2.5^\circ \times 2.5^\circ$ horizontal resolution and total cloud cover (entire atmosphere
103 considered as a single layer; 192×94 points in the horizontal direction), from the National
104 Centers for Environmental Prediction (NCEP)–National Center for Atmospheric Research (NCAR)
105 Reanalysis I (NCEP/NCAR) (Kalnay et al., 1996); (3) monthly mean SST, with a $2^\circ \times 2^\circ$
106 horizontal resolution, of the Extended Reconstructed SST dataset, version 5 (ERSST.v5; Huang et
107 al., 2017), from the National Oceanic and Atmospheric Administration (NOAA); (4) global
108 monthly precipitation data, with a $2.5^\circ \times 2.5^\circ$ horizontal resolution, from NOAA’s precipitation
109 reconstruction (Chen et al., 2002); (5) ground-timing observation datasets, at 02:00, 08:00, 14:00
110 and 20:00 BLT (Beijing local time), from the National Meteorological Information Center of
111 China. The temporal coverage of the PBLH data is from 1979 to 2017, while the remaining
112 datasets are from 1960 to 2017. Here, boreal autumn refers to the seasonal mean for September–
113 October–November (SON).

114

115 **2.2 Model**

116 The numerical model we employed is an anomaly atmospheric general circulation model (AGCM)
117 based on the Geophysical Fluid Dynamics Laboratory (GFDL) global spectrum dry AGCM (Held
118 and Suarez, 1994). The horizontal resolution is T42, with five evenly spaced sigma levels ($\sigma =$
119 p/ps ; interval: 0.2; top level: $\sigma = 0$; bottom level: $\sigma = 1$). A realistic autumn mean state, obtained
120 from the long-term mean of the NCEP/NCAR reanalysis data, is prescribed as the model basic
121 state. This model has been used to unravel the eddy–mean interaction over East Asia and its
122 downstream climate impacts over North America (Zhu and Li, 2016, 2018).

123

124 **2.3 Methodology**

125 The definition of a haze day in the present study is identical to the previous studies (e.g., Chen and
126 Wang, 2015). It is based on the ground-timing observations of relative humidity, visibility and
127 wind speed. It is important to point out that the visibility observations switched from manual to
128 automatic in 2014, and the visibility threshold for haze was thus also slightly modified from then
129 on. Nevertheless, the continuity of the data was not affected. Following Zhang et al. (2016), the
130 mean number of haze days ($\overline{\text{NHD}}$) for AHD_{BTH} was computed by:

131
$$\overline{\text{NHD}} = \frac{1}{n} \sum_{i=1}^n N \quad (1)$$

132 where n (here, $n = 20$) is the number of meteorological sites distributed within the BTH region
133 (Fig. 1), and N denotes the number of haze days at a site for each autumn.

134 Similar to the approach proposed by Zhu and Li (2017), the 9-yr running mean of the AHD_{BTH}
135 was used to represent the interdecadal component of the AHD_{BTH} , whereas the interannual
136 component was obtained by removing the interdecadal component from the raw AHD_{BTH} . Since
137 there is a tapering problem when calculating the running mean, the first four years and the last

138 four years of the interdecadal component of the AHD_{BTH} could be estimated by the mean value of
139 the available data with a shorter window. For example, the interdecadal component of the AHD_{BTH}
140 for 2016 and 2017 could be obtained by the mean of 2012–17 and 2013–17, respectively. Note
141 that the temporal correlation coefficients (TCCs) between the AHD_{BTH} and every single stations
142 were all positive and significant (Fig. 1), indicating the coherency of the interannual variability of
143 autumnal haze days in each station over the BTH region; meanwhile, the distribution of these
144 stations was fairly even. Therefore, the interannual component of the AHD_{BTH} could be a good
145 representation of the year-to-year pollution state over the whole BTH region in autumn.

146 Linear regression, composite analysis and correlation were used to examine the circulation and
147 SST anomalies that associated with the interannual AHD_{BTH} . The two-tailed Student's *t*-test was
148 employed to evaluate the statistical significance of these analyses. The wave activity flux (WAF;
149 Takaya and Nakamura, 2001) was calculated to depict the tendency of Rossby wave energy
150 propagation.

151

152 **3 Atmospheric anomalies associated with the interannual changes of AHD_{BTH}**

153 Figure 2 illustrates the time series of the raw AHD_{BTH} , along with its interdecadal and interannual
154 components. A prominent feature is that the AHD_{BTH} displays both interannual and interdecadal
155 variability. On the interdecadal timescale, the AHD_{BTH} was below average during 1960–1975 and
156 the late-2000s, but above average during 1975–2003, and it increased dramatically after 2009. On
157 the interannual timescale, the AHD_{BTH} presents large differences year by year. For example, the
158 AHD_{BTH} was at its lowest in 2012, but peaked in 2014. Since the interannual variability explains
159 most of the total variances in the AHD_{BTH} variability, in this study we investigate the atmospheric
160 anomalies and unravel the underlying physical processes that associated with the AHD_{BTH} on the
161 interannual timescale.

162 Close scrutiny of the large-scale and localized dynamic and thermodynamic fields associated with
163 the AHD_{BTH} could advance our understanding of the underlying mechanisms. In this regard, we
164 firstly examine the climatological mean autumnal 500-hPa geopotential height (Z500), 850-hPa
165 winds (UV850) and total cloud, along with the surface relative humidity and surface air
166 temperature that potentially impact the climate over the BTH region (Fig. 3). There is a shallow
167 mid-tropospheric trough over coastal East Asia (Fig. 3a), which resembles the trough in winter
168 (Zhao et al., 2018; Pei et al., 2018) but with a smaller magnitude. Behind the trough, a clear
169 anticyclonic circulation appears over the central-eastern China, with remarkable
170 westerly/northwesterly winds dominating the BTH region (Fig. 3a). Cool and dry air from higher
171 latitudes is advected by the winds, and the BTH region is thus much cooler and drier and has less
172 cloud than other regions at the same latitudes (e.g., the central Japan). As such, the autumnal BTH
173 region features breezy and windy conditions, with low surface relative humidity (Fig. 3b),
174 reducing the likelihood of haze there via the effect of cold advection and ventilation effect. Note,
175 however, that if the breezy conditions are interrupted, haze pollution is likely to occur. One may
176 ask whether a higher AHD_{BTH} is related to the interference of such breezy conditions. Figures 4
177 and 5 were therefore plotted to examine the associated atmospheric parameters/circulations. For
178 simplicity, the regression and composite analyses in this study reported hereafter are interpreted
179 with respect to positive phase of AHD_{BTH} anomalies only.

180 Previous studies have revealed that haze pollution is closely correlated with local meteorological
181 parameters in the planetary boundary layer (e.g., You et al., 2017; Chen et al., 2018). Figure 4
182 suggests that an above-normal AHD_{BTH} is tied to a localized increase of surface relative humidity
183 (Fig. 4a) and surface air temperature (Fig. 4b), along with suppressed surface wind speed (Fig. 4c),

184 sea-level pressure (SLP) (Fig. 4d) and PBLH (Fig. 4e).. The question is, what causes the above
185 anomalous parameters that are favorable for a higher AHD_{BTH} ?

186 Figure 5 shows the associated large-scale atmospheric circulation anomalies at different levels of
187 troposphere. In Figs. 5a–5d, the most noticeable feature is that there is a planetary-scale,
188 quasi-barotropic Rossby wave train emanating from the North Atlantic subtropical sector. In
189 addition to an anticyclonic anomaly centered over the North Atlantic subtropics, this
190 teleconnection pattern has another two pairs of anomalous cyclones (low pressure) and
191 anticyclones (high pressure) stretching across Eurasia to the Northeast Asia, i.e., a cyclonic
192 anomaly centered over the ocean south of Greenland, an anticyclonic anomaly centered over
193 Scandinavia, a cyclonic anomaly centered over the adjacent central Siberia, and an anticyclonic
194 anomaly centered over the Sea of Japan (SJ). In general, based on the regressed atmospheric fields,
195 the teleconnection has a much larger amplitude in the upper troposphere (Fig. 5a) than that in the
196 mid-troposphere (Fig. 5b) and lower troposphere (Fig. 5c). Intriguingly, from the surface
197 projection of the above quasi-barotropic teleconnection pattern, we can discern a positive phase of
198 North Atlantic Oscillation -like mode in connection with this pattern (Hurrell and Deser, 2009).

199 Among all the height anomalies within the teleconnection, the anomalous quasi-barotropic
200 Northeast Asian anticyclonic anomaly centered over the SJ (A_{SJ}) plays a direct role in driving a
201 higher AHD_{BTH} . The related physical-meteorological causes are as follows: There are
202 southerly/southeasterly anomalies along the western flank of the A_{SJ} in the lower troposphere (Figs.
203 5c and 5d), manifesting the capability of suppressed atmospheric horizontal diffusion and thus
204 favoring a buildup of substantial local and nonlocal APs and warmer moisture over the BTH
205 region (Yang et al., 2015; Yang et al., 2016) under the specific topographical forcing of the
206 Taihang Mountains and Yan Mountains (Fig. 1). On the other hand, the significant positive
207 pressure anomaly in the mid-to-upper parts of the A_{SJ} (Figs. 5a and 5b) not only impedes the
208 intrusion of cold air into the BTH region, but also facilitates consistent air subsidence over the
209 BTH region and its surrounding areas (Fig. 4f), resulting in the decrease of the PBLH and increase
210 of static stability (i.e., the dampened vertical dispersion of the atmosphere). Consequently, the
211 meteorological conditions connected to a higher AHD_{BTH} are adverse to the autumn climate mean
212 state (Fig. 3).

213 To summarize, the A_{SJ} and the associated subsidence can induce the capacity for suppressed local
214 horizontal and vertical dispersion over the BTH region and its surrounding areas, as shown in the
215 above-mentioned anomalous parameters (Fig. 4); and these parameters are further responsible for
216 the accumulation and secondary formation/hygroscopic growth of APs (Jacob and Winner, 2009;
217 Ding and Liu, 2014; Mu and Liao, 2014; Jia et al., 2015). As such, the haze pollution over the
218 BTH region is readily established within a narrow space. Therefore, the question of how the
219 above-normal AHD_{BTH} is stimulated could plausibly be transferred into how the A_{SJ} is developed
220 and sustained. In fact, the A_{SJ} and the associated air subsidence are modulated by remote SSTAs.
221 We tackle the underlying mechanisms in the next section.

222

223 **4 Mechanisms of the A_{SJ}**

224

225 **4.1 Observational diagnoses**

226 Figure 5c shows that an above-normal AHD_{BTH} is closely correlated with SST warming in two key
227 regions: One is the North Atlantic subtropical sector (R1: 22° – 32° N, 90° – 40° W), and the other is
228 the western North Pacific sector (R2: 10° – 30° N, 108° – 140° E), with its southern portion belonging

229 to the Western Pacific Warm Pool (You et al., 2018). One may ask why we chose these two key
230 SSTA regions. Firstly, the subtropical North Atlantic SSTA is the only region over North Atlantic
231 that highly correlated with the AHD_{BTH} on interannual timescale. Although the regression SSTA
232 pattern over North Atlantic looks like a tri-pole SST pattern which has profound impacts on
233 Eurasian climate, the relationship between AHD_{BTH} and simultaneous NAT SST pattern is
234 insignificant. The correlation coefficient between AHD_{BTH} and NAT SST triple-pole index (Deser
235 and Michael, 1997) is only 0.17. Therefore, we chose the middle oceanic region of North Atlantic
236 as the key region for AHD_{BTH} . Secondly, the positive correlated SSTA over R1 and R2 region can
237 both induce positive rainfall anomaly (diabatic heating), the SSTA should play an active role in
238 local air-sea interaction and in turn influence the large-scale circulation. Therefore, we chose the
239 R1 and R2 as the key SSTA regions from both statistical diagnosis and physical basis. Figure 6
240 further depicts that the SON SSTs over both R1 and R2 are positively correlated with AHD_{BTH} ,
241 and the TCC between the AHD_{BTH} and SON SST over R1 (R2) is 0.45 (0.28), exceeding the 99%
242 (95%) confidence level. By virtue of the above analyses, we speculate that the SST over R1 may
243 play a more important role than that over R2 in driving a higher AHD_{BTH} . Note, however, that
244 when the SON SSTs over R1 and R2 are both obviously elevated, the AHD_{BTH} is more likely to be
245 higher than normal, such as in 1980, 1987 and 2015. As indicated above, the AHD_{BTH} is closely
246 correlated with the A_{SJ} and the associated air subsidence, which allows us to speculate that the
247 positive SSTAs over R1 and R2 might drive the interannual variability of AHD_{BTH} by modulating
248 the intensity of the A_{SJ} and associated subsidence. To validate this hypothesis, we firstly examine
249 the pathway of SSTAs over R1 in driving AHD_{BTH} .

250 Figure 5c suggests that the SST warming in R1 may induce larger-area low-level easterly
251 anomalies to its east, leading to anticyclonic wind shear over this region. In such a scenario, an
252 anticyclonic anomaly is induced (Fig. 5c), with its center to the northeast of R1. Along the western
253 flank of this anticyclonic anomaly, warm and moist airflows move northwards. When these warm
254 and moist airflows meet cold air mass in the areas to the north of R1, enhanced precipitation is
255 thus generated (Fig. 5e). Meanwhile, the resultant enhanced rainfall condensation heating induces
256 a cyclonic anomaly to its north, thereby exciting the other two pairs of the aforementioned
257 teleconnection pattern along the westerly jet, as demonstrated by the Rossby wave train induced
258 by SST warming in R1 (Figs. 7 and 8). Specifically, from the regressed SON UV850 (Fig. 7), we
259 can see that the SST warming in R1 can indeed induce a significant low-level teleconnection
260 pattern arising from the North Atlantic subtropics, bearing a close resemblance to that in Fig. 5c;
261 and to the north of R1, where the rainfall condensation heating is triggered, the corresponding
262 WAF exhibits a distinctive arc-shaped trajectory, perturbing the other two pairs of cyclones and
263 anticyclones of the teleconnection (Fig. 8). This teleconnection extends from the North Atlantic
264 towards Scandinavia, goes through the Eurasia and arrives at the Northeast Asia. Therefore, by
265 means of this trajectory, Rossby wave energy in the middle (Fig. 8b) and upper (Fig. 8a)
266 troposphere may propagate southeastwards into the A_{SJ} and its surrounding region, favoring the
267 formation/sustainability of the A_{SJ} and the associated air subsidence. In this context, the associated
268 meteorological parameters (Fig. S1), which resemble those tied to a higher AHD_{BTH} (Fig. 4),
269 might increase the likelihood of SON haze pollution over the BTH region. Again, this induced
270 teleconnection is quasi-barotropic in structure, with its magnitude larger in the upper troposphere
271 (Fig. 8a), which is consistent with that in Fig. 5a.

272 As for the role of R2 SSTA warming (Fig. 9a), we find that, corresponding to the SSTAs over R2,
273 there exists a cyclonic anomaly to the west of R2. Besides, substantial SSTA-induced low-level
274 easterly anomalies are appeared to the southeast of R2; meanwhile, a large-scale anticyclonic
275 anomaly to the northeast is excited, with its center situated over the northern Pacific. In such a
276 scenario, R2 is thoroughly controlled by significant warm and humid airflows transported from the

277 eastern flank of the cyclonic and the western flank of anticyclonic anomaly respectively (Fig. 9a).
278 Furthermore, the airflow convergence primarily occurs over the southwestern portion of R2,
279 where the strongly significant and positive rainfall anomaly is triggered (Fig. 9b). Thus, the
280 enhanced significant rainfall heating may greatly intensify the ascending motion over R2 and the
281 adjacent region, resulting in subsidence over the BTH region and Northeast Asia via an anomalous
282 local meridional cell (Fig. 10a). As such, the BTH region is dominated by significant warm
283 temperatures in the middle and upper troposphere (Fig. 10b); and the A_{SJ} , the downward motions
284 over the BTH region as well as the regional low-level stability over BTH, are maintained and
285 reinforced. Under such circumstances, the vertical transport of APs is restricted (Zhang et al., 2014;
286 Pei et al., 2018), and the near-surface winds are weakened (Li et al., 2016). The parameters
287 associated with SST warming in R2 (Fig. S2) also support the formation of haze weather over the
288 BTH region.

289

290 4.2 Numerical model simulations

291 Two experiments were conducted to further validate the above-mentioned two pathways of how
292 SSTAs drive the variation of AHD_{BTH} . The first experiment (H_{NAS}) simulated the responses to
293 the heating induced by SSTAs over R1 (Fig. 11). H_{NAS} was imposed with a specified heating
294 centered over the region to the north of R1 (center: 37.67°N, 64.69°W) that largely matched with
295 the SON positive rainfall anomaly as shown in Fig. 5e. The second experiment (H_{WNP})
296 mimicked the responses to the prescribed heating over the neighboring areas of R2 (center:
297 15.35°N, 109.69°E; Fig. 12), where the corresponding regressed precipitation rate was the most
298 significant, as exhibited in Fig. 9b. The heating had a cosine-squared profile in an elliptical region
299 in the horizontal direction. The maximum heating, with 1 K day⁻¹ amplitude, was set to be at 300
300 hPa.

301 Figure 11 presents the 200- and 500-hPa geopotential height and wind responses to the specified
302 heating over the North Atlantic subtropical region. As anticipated, the equilibrium state (mean
303 output from day 40 to day 60) of the Z200 (Fig. 11a) and Z500 (Fig. 11b) responses to the heating
304 resembles the aforementioned teleconnection (Figs. 5a and 5b), and the simulated response of the
305 Z200 anomalies is generally larger than its counterpart at 500 hPa (Fig. 11b), which concurs with
306 the observational evidence. Besides, a similar low-level portion of the A_{SJ} could also be simulated
307 (figure not shown). As a result, a strengthened A_{SJ} is induced.

308 Figure 12 delineates the 850-hPa geopotential height (Z850) and UV850 responses to the specified
309 heating centered at (15.35°N, 109.69°E). Although there are some differences in spatial
310 distribution compared with the observations, the well-organized cyclonic anomaly to the west of
311 the heating center and the anticyclonic anomaly over Northeast Asia can be well simulated (Fig.
312 12). Meanwhile, the A_{SJ} and the coherent tropospheric subsidence over the BTH region and the
313 Northeast Asian anticyclonic anomaly were also simulated well (figure not shown).

314 To sum up, from observational diagnoses and numerical simulations, we can conclude that there
315 are two pathways regarding how remote SSTAs impact the formation and maintenance of the A_{SJ}
316 and the associated air subsidence. One pathway operates via a heating-induced large-scale
317 teleconnection pattern arising from SST warming in R1, and the other is connected to an
318 anomalous local meridional cell triggered by heating-reinforced ascending motion via local SST
319 warming over R2.

320

321

322 5 Conclusions and discussion

323 Motivated by a lack of in-depth understanding with respect to the interannual variations of the
324 AHD_{BTH} , in the present study we explored the related climate anomalies (localized meteorological
325 parameters, and large-scale atmospheric and oceanic anomalies) tied to the AHD_{BTH} . We have
326 substantiated that an above-normal AHD_{BTH} is closely correlated with the simultaneous SST
327 warming in two key regions (R1 over the North Atlantic subtropical sector, and R2 over the
328 western North Pacific sector), and once the SON SST warming in R1 and R2 are both remarkably
329 significant, their joint climate impacts can greatly enhance the likelihood of an above-normal
330 AHD_{BTH} .

331 Potential mechanisms associated with an above-normal AHD_{BTH} have been proposed through
332 further investigations. Since the A_{SJ} and the associated subsidence over the A_{SJ} and the
333 surrounding region can yield meteorological circumstances conducive to enhancing the likelihood
334 of haze pollution in the BTH region, the issue of an above-normal AHD_{BTH} can be reasonably
335 transferred into uncovering how the SON A_{SJ} and associated air subsidence are developed and
336 sustained. We found that there are two possible pathways. First, SST warming in R1 can induce a
337 downstream Rossby wave teleconnection, and the associated Rossby wave energy can propagate
338 into Northeast Asia through an arc-shaped trajectory, developing and strengthening the A_{SJ} and the
339 associated subsidence over BTH. The other pathway, however, operates through localized
340 heating-reinforced ascending motion over R2, also resulting in subsidence over the BTH region
341 via an anomalous local meridional cell.

342 AGCM simulations supported our hypothesis. With prescribed heating over the region to the north
343 of R1, a quite similar teleconnection—starting from the North Atlantic subtropics—was excited. If
344 we imposed an idealized heating over the adjacent R2, where the corresponding precipitation rate
345 was the most significant, the significant low-level convergence around the heated areas was
346 simulated, inducing the A_{SJ} -resembled circulation to the north and the subsidence over the BTH
347 region. However, because the model we used is an intermediate anomaly AGCM, and the heating
348 prescribed in the model is idealized, the simulated patterns were slightly spatially different to
349 those observed. Although the model cannot reproduce the geopotential height and wind anomalies
350 perfectly, it can still support our proposed mechanisms. As a summary, a schematic illustration
351 (Fig. 13) of the occurrence of a higher AHD_{BTH} is provided, which encapsulates the major
352 characteristics of the two pathways of how remote SSTAs over R1 and R2 drive the AHD_{BTH}
353 respectively.

354 From the perspective of seasonal prediction, among all the previous individual months of boreal
355 summer (June–July–August), the SON SST in R1 (R2) was most significantly correlated with the
356 August SST in R1 (R2) on the interannual timescale, with a TCC of 0.35 (0.61) that exceeded the
357 95% (99%) confidence level. This suggests that, when the August SST over R1 (R2) is higher, the
358 subsequent SON SST over R1 (R2) is more likely to become warmer. As such, the previous
359 August SSTA over R1 (R2) could serve as a possible precursor for the seasonal prediction of the
360 AHD_{BTH} .

361 In this study, we solely emphasize the potential impacts of SSTAs on the interannual variations of
362 the AHD_{BTH} . It should be noted that other external forcings, such as the Arctic sea ice (e.g., Wang
363 et al., 2015), Eurasian snowpack, thermal conditions on the Tibetan Plateau (e.g., Xu et al., 2016)
364 and soil moisture, may also exert profound impacts on haze pollution over China. Studying the
365 mechanisms tied to these forcings may enhance the seasonal predicting skill for the AHD_{BTH} .
366 Meanwhile, in this study, we only focus on the variability of AHD_{BTH} on interannual timescale.

367 Whether the proposed mechanism of AHD_{BTH} is still at play on intraseasonal timescale? Is it
368 possible for making an extended-range forecast of the occurrence of haze days? These topics are
369 of both scientific and practical importance, and merit further explorations.

370

371

372 *Data availability.* The atmospheric data and land-surface data are available from the NCEP/NCAR data archive:
373 <http://www.esrl.noaa.gov/psd/data/gridded/data.ncep.reanalysis.html> (NCEP/NCAR, 2018). The SST data were downloaded from
374 <https://www.esrl.noaa.gov/psd/data/gridded/data.noaa.ersst.v5.html> (NOAA, 2018). The precipitation data were downloaded from
375 <https://www.esrl.noaa.gov/psd/data/gridded/data.prec.html> (NOAA, 2018). The monthly PBLH data are available on the ERA-Interim
376 website: <http://www.ecmwf.int/en/research/climate-reanalysis/era-interim> (ERA-Interim, 2018). The ground observations are from the
377 National Meteorological Information Center of China (<http://data.cma.cn/>) (CMA, 2018).

378 *Competing interests.* The authors declare that they have no conflict of interest.

379 *Author contributions.* JW analyzed the observational data, ZZ and JW designed the numerical experiments. JW and ZZ wrote the
380 manuscript. LQ, QZ, JH and JXW were involved in the scientific interpretation and discussion.

381 *Acknowledgements.* This work was supported by the National Key Research and Development Program of China (Grants
382 2018YFC1505905 and 2018YFC1505803), and the National Natural Science Foundation of China (Grant 41605035).

383

384

385

386

387

388

389

390

391

392

393

394

395

396

397

398

399

400

401

402

403

404

405

406

407

408

409

410 **References**

- 411 Cai, W. J., Li, K., Liao, H., Wang, H. J., and Wu, L. X.: Weather conditions conducive to Beijing severe haze more
412 frequent under climate change, *Nat Clim Change*, 7, 257-262, 10.1038/nclimate3249, 2017.
- 413 Cao, J. J., Lee, S. C., Chow, J. C., Watson, J. G., Ho, K. F., Zhang, R. J., Jin, Z. D., Shen, Z. X., Chen, G. C., Kang,
414 Y. M., Zou, S. C., Zhang, L. Z., Qi, S. H., Dai, M. H., Cheng, Y., and Hu, K.: Spatial and seasonal distributions
415 of carbonaceous aerosols over China, *J Geophys Res Atmos*, 112, D22S11, 10.1029/2006JD008205, 2007.
- 416 Chameides, W. L., Yu, H., Liu, S. C., Bergin, M., Zhou, X., Mearns, L., Wang, G., Kiang, C. S., Saylor, R. D., Luo,
417 C., Huang, Y., Steiner, A., and Giorgi, F.: Case study of the effects of atmospheric aerosols and regional haze on
418 agriculture: An opportunity to enhance crop yields in China through emission controls?, *Proceedings of the*
419 *National Academy of Sciences*, 96, 13626, 1999.
- 420 Charlson, R. J., Schwartz, S. E., Hales, J. M., Cess, R. D., Coakley Jr, J. A., Hansen, J. E., and Hofmann, D. J.:
421 Climate forcing by anthropogenic aerosols, *Science*, 255, 423-430, 10.1126/science.255.5043.423, 1992.
- 422 Chen, H. P., and Wang, H. J.: Haze Days in North China and the associated atmospheric circulations based on daily
423 visibility data from 1960 to 2012, *J Geophys Res Atmos*, 120, 5895-5909, 10.1002/2015JD023225, 2015.
- 424 Chen, J., Zhao, C. S., Ma, N., Liu, P. F., Göbel, T., Hallbauer, E., Deng, Z. Z., Ran, L., Xu, W. Y., Liang, Z., Liu, H.
425 J., Yan, P., Zhou, X. J., and Wiedensohler, A.: A parameterization of low visibilities for hazy days in the North
426 China Plain, *Atmos Chem Phys*, 12, 4935-4950, 10.5194/acp-12-4935-2012, 2012.
- 427 Chen, M. Y., Xie, P. P., Janowiak, J. E., and Arkin, P. A.: Global land precipitation: A 50-yr monthly analysis based
428 on gauge observations, *J Hydrometeorol*, 3, 249-266, 10.1175/1525-7541(2002)003<0249:glpaym>2.0.co;2, 2002.
- 429 Chen, Y. N., Zhu, Z. W., Luo, L., and Zhang, J. W.: Severe haze in Hangzhou in winter 2013/14 and associated
430 meteorological anomalies, *Dyn Atmos Oceans*, 81, 73-83, 10.1016/j.dynatmoce.2018.01.002, 2018.
- 431 Chen, Y. Y., Ebenstein, A., Greenstone, M., and Li, H. B.: Evidence on the impact of sustained exposure to air
432 pollution on life expectancy from China's Huai River policy, *Proc Natl Acad Sci*, 110, 12936-12941,
433 10.1073/pnas.1300018110, 2013.
- 434 Chen, Z. Y., Xie, X. M., Cai, J., Chen, D. L., Gao, B. B., He, B., Cheng, N. L., and Xu, B.: Understanding
435 meteorological influences on PM_{2.5} concentrations across China: a temporal and spatial perspective, *Atmos*
436 *Chem Phys*, 18, 5343-5358, 10.5194/acp-18-5343-2018, 2018.
- 437 Chung, C. E., Ramanathan, V., and Kiehl, J. T.: Effects of the South Asian absorbing haze on the Northeast
438 monsoon and surface-air heat exchange, *J Climate*, 15, 2462-2476,
439 10.1175/1520-0442(2002)015<2462:eotsaa>2.0.co;2, 2002.
- 440 CMA: China ground observation data sets, available at: <http://data.cma.cn/>, last access: 10 January 2018 (in
441 Chinese).
- 442 Dee, D. P., Uppala, S. M., Simmons, A. J., Berrisford, P., Poli, P., Kobayashi, S., Andrae, U., Balmaseda, M. A.,
443 Balsamo, G., Bauer, P., Bechtold, P., Beljaars, A. C. M., van de Berg, L., Bidlot, J., Bormann, N., Delsol, C.,
444 Dragani, R., Fuentes, M., Geer, A. J., Haimberger, L., Healy, S. B., Hersbach, H., Hólm, E. V., Isaksen, I.,
445 Kållberg, P., Köhler, M., Matricardi, M., McNally, A. P., Monge-Sanz, B. M., Morcrette, J. J., Park, B. K.,
446 Peubey, C., de Rosnay, P., Tavolato, C., Thépaut, J. N., and Vitart, F.: The ERA-Interim reanalysis: configuration
447 and performance of the data assimilation system, *Q J R Meteorol Soc*, 137, 553-597, 10.1002/qj.828, 2011.
- 448 Deser, C. and Michael S.T.: Atmosphere-ocean interaction on weekly timescales in the North Atlantic and Pacific.
449 *Journal of Climate*, 10(3): 393-408, 1997.

450 Ding, Y. H., and Liu, Y. J.: Analysis of long-term variations of fog and haze in China in recent 50 years and their
451 relations with atmospheric humidity, *Sci China Earth Sci*, 57, 36-46, 10.1007/s11430-013-4792-1, 2014.

452 Ding, Y. H., Wu, P., Liu, Y. J., and Song, Y. F.: Environmental and dynamic conditions for the occurrence of
453 persistent haze events in North China, *Engineering*, 3, 266-271, 10.1016/J.ENG.2017.01.009, 2017.

454 ERA-Interim: PBLH data sets, available at: <http://www.ecmwf.int/en/research/climate-reanalysis/era-interim>, last
455 access: 10 January 2018.

456 Gao, H., and Li, X.: Influences of El Nino Southern Oscillation events on haze frequency in eastern China during
457 boreal winters, *Int J Climatol*, 35, 2682-2688, 10.1002/joc.4133, 2015.

458 Gao, Y., and Chen, D.: A dark October in Beijing 2016, *Atmos Oceanic Sci Lett*, 10, 206-213,
459 10.1080/16742834.2017.1293473, 2017.

460 Guo, J. P., Zhang, X. Y., Wu, Y. R., Zhaxi, Y. Z., Che, H. Z., La, B., Wang, W., and Li, X. W.: Spatio-temporal
461 variation trends of satellite-based aerosol optical depth in China during 1980–2008, *Atmos Environ*, 45,
462 6802-6811, 10.1016/j.atmosenv.2011.03.068, 2011.

463 Guo, S., Hu, M., Zamora, M. L., Peng, J. F., Shang, D. J., Zheng, J., Du, Z. F., Wu, Z. J., Shao, M., Zeng, L. M.,
464 Molina, M. J., and Zhang, R. Y.: Elucidating severe urban haze formation in China, *Proc Natl Acad Sci*, 111,
465 17373-17378, 10.1073/pnas.1419604111, 2014.

466 He, J. H., and Zhu, Z. W.: The relation of South China Sea monsoon onset with the subsequent rainfall over the
467 subtropical East Asia, *Int J Climatol*, 35, 4547-4556, 10.1002/joc.4305, 2015.

468 Held, I. M., and Suarez, M. J.: A proposal for the intercomparison of the dynamical cores of atmospheric general
469 circulation models, *Bull Amer Meteor Soc*, 75, 1825-1830, 10.1175/1520-0477(1994)075<1825:apftio>2.0.co;2,
470 1994.

471 Huang, B. Y., Thorne, P. W., Banzon, V. F., Boyer, T., Chepurin, G., Lawrimore, J. H., Menne, M. J., Smith, T. M.,
472 Vose, R. S., and Zhang, H. M.: Extended Reconstructed Sea Surface Temperature, version 5 (ERSSTv5):
473 Upgrades, validations, and intercomparisons, *J Climate*, 30, 8179-8205, 10.1175/jcli-d-16-0836.1, 2017.

474 Hurrell, J. W., and Deser, C.: North Atlantic climate variability: The role of the North Atlantic Oscillation, *J
475 Marine Syst*, 78, 28-41, 10.1016/j.jmarsys.2008.11.026, 2009.

476 Jacob, D. J., and Winner, D. A.: Effect of Climate Change on Air Quality, *Atmos Environ*, 43, 51-63,
477 10.1016/j.atmosenv.2008.09.051, 2009.

478 Jia, B., Wang, Y., Yao, Y., and Xie, Y.: A new indicator on the impact of large-scale circulation on wintertime
479 particulate matter pollution over China, *Atmos Chem Phys*, 15, 11919-11929, 10.5194/acp-15-11919-2015,
480 2015.

481 Kalnay, E., Kanamitsu, M., Kistler, R., Collins, W., Deaven, D., Gandin, L., Iredell, M., Saha, S., White, G.,
482 Woollen, J., Zhu, Y., Leetmaa, A., Reynolds, R., Chelliah, M., Ebisuzaki, W., Higgins, W., Janowiak, J., Mo, K.
483 C., Ropelewski, C., Wang, J., Jenne, R., and Joseph, D.: The NCEP/NCAR 40-year reanalysis project, *Bull
484 Amer Meteor Soc*, 77, 437-471, 10.1175/1520-0477(1996)077<0437:tnyrp>2.0.co;2, 1996.

485 Lau, K. M., and Kim, K. M.: Observational relationships between aerosol and Asian monsoon rainfall, and
486 circulation, *Geophys Res Lett*, 33, L21810, 10.1029/2006GL027546, 2006.

487 Lau, K. M., Kim, M. K., and Kim, K. M.: Asian summer monsoon anomalies induced by aerosol direct forcing: the
488 role of the Tibetan Plateau, *Clim Dyn*, 26, 855-864, 10.1007/s00382-006-0114-z, 2006.

- 489 Li, C., Martin, R. V., Boys, B. L., van Donkelaar, A., and Ruzzante, S.: Evaluation and application of multi-decadal
490 visibility data for trend analysis of atmospheric haze, *Atmos Chem Phys*, 16, 2435-2457,
491 10.5194/acp-16-2435-2016, 2016.
- 492 Li, Q., Zhang, R. H., and Wang, Y.: Interannual variation of the wintertime fog–haze days across central and
493 eastern China and its relation with East Asian winter monsoon, *Int J Climatol*, 36, 346-354, 10.1002/joc.4350,
494 2016.
- 495 Li, R., Hu, Y. J., Li, L., Fu, H. B., and Chen, J. M.: Real-time aerosol optical properties, morphology and mixing
496 states under clear, haze and fog episodes in the summer of urban Beijing, *Atmos Chem Phys*, 17, 5079-5093,
497 10.5194/acp-17-5079-2017, 2017.
- 498 Li, Z. Q., Lau, W. K. M., Ramanathan, V., Wu, G., Ding, Y., Manoj, M. G., Liu, J., Qian, Y., Li, J., Zhou, T., Fan, J.,
499 Rosenfeld, D., Ming, Y., Wang, Y., Huang, J., Wang, B., Xu, X., Lee, S. S., Cribb, M., Zhang, F., Yang, X., Zhao,
500 C., Takemura, T., Wang, K., Xia, X., Yin, Y., Zhang, H., Guo, J., Zhai, P. M., Sugimoto, N., Babu, S. S., and
501 Brasseur, G. P.: Aerosol and monsoon climate interactions over Asia, *Rev Geophys*, 54, 866-929,
502 10.1002/2015RG000500, 2016.
- 503 Liu, Y., Sun, J. R., and Yang, B.: The effects of black carbon and sulphate aerosols in China regions on East Asia
504 monsoons, *Tellus B*, 61, 642-656, 10.1111/j.1600-0889.2009.00427.x, 2009.
- 505 Luan, T., Guo, X. L., Guo, L. J., and Zhang, T. H.: Quantifying the relationship between PM_{2.5} concentration,
506 visibility and planetary boundary layer height for long-lasting haze and fog–haze mixed events in Beijing,
507 *Atmos Chem Phys*, 18, 203-225, 10.5194/acp-18-203-2018, 2018.
- 508 Mu, M., and Zhang, R. H.: Addressing the issue of fog and haze: A promising perspective from meteorological
509 science and technology, *Sci China Earth Sci*, 57, 1-2, 10.1007/s11430-013-4791-2, 2014.
- 510 Mu, Q., and Liao, H.: Simulation of the interannual variations of aerosols in China: role of variations in
511 meteorological parameters, *Atmos Chem Phys*, 14, 9597-9612, 10.5194/acp-14-9597-2014, 2014.
- 512 NCEP/NCAR: NCEP/NCAR Reanalysis data sets, available at: <http://www.esrl.noaa.gov/psd/data>
513 [/gridded/data.ncep.reanalysis.html](http://www.esrl.noaa.gov/psd/data/gridded/data.ncep.reanalysis.html), last access: 10 January 2018.
- 514 Niu, F., Li, Z. Q., Li, C., Lee, K. H., and Wang, M. Y.: Increase of wintertime fog in China: Potential impacts of
515 weakening of the Eastern Asian monsoon circulation and increasing aerosol loading, *J Geophys Res*, 115,
516 D00K20, 10.1029/2009JD013484, 2010.
- 517 NOAA: NOAA Extended Reconstructed Sea Surface Temperature (SST) V5 data sets, available at:
518 <https://www.esrl.noaa.gov/psd/data/gridded/data.noaa.ersst.v5.html>, last access: 10 January 2018.
- 519 NOAA: NOAA precipitation datasets, available at: <https://www.esrl.noaa.gov/psd/data/gridded/data.prec.html>,
520 last access: 10 January 2018.
- 521 Pei, L., Yan, Z. W., Sun, Z. B., Miao, S. G., and Yao, Y.: Increasing persistent haze in Beijing: potential impacts of
522 weakening East Asian winter monsoons associated with northwestern Pacific sea surface temperature trends,
523 *Atmos Chem Phys*, 18, 3173–3183, 10.5194/acp-18-3173-2018, 2018.
- 524 Pope III, C. A., and Dockery, D. W.: Health effects of fine particulate air pollution: Lines that connect, *J Air Waste*
525 *Manage*, 56, 709-742, 10.1080/10473289.2006.10464485, 2006.
- 526 Seo, J., Kim, J. Y., Youn, D., Lee, J. Y., Kim, H., Lim, Y. B., Kim, Y., and Jin, H. C.: On the multiday haze in the
527 Asian continental outflow: the important role of synoptic conditions combined with regional and local sources,
528 *Atmos Chem Phys*, 17, 9311-9332, 10.5194/acp-17-9311-2017, 2017.

- 529 Takaya, K., and Nakamura, H.: A formulation of a phase-independent wave-activity flux for stationary and
530 migratory quasigeostrophic eddies on a zonally varying basic flow, *J Atmos Sci*, 58, 608-627,
531 10.1175/1520-0469(2001)058<0608:afopi>2.0.co;2, 2001.
- 532 Tao, M. H., Chen, L. F., Xiong, X. Z., Zhang, M. G., Ma, P. F., Tao, J. H., and Wang, Z. F.: Formation process of
533 the widespread extreme haze pollution over northern China in January 2013: Implications for regional air
534 quality and climate, *Atmos Environ*, 98, 417-425, 10.1016/j.atmosenv.2014.09.026, 2014.
- 535 Tao, M. H., Chen, L. F., Wang, Z. F., Wang, J., Tao, J. H., and Wang, X. H.: Did the widespread haze pollution over
536 China increase during the last decade? A satellite view from space, *Environ Res Lett*, 11, 054019,
537 10.1088/1748-9326/11/5/054019, 2016.
- 538 Tett, S. F. B., Stott, P. A., Allen, M. R., Ingram, W. J., and Mitchell, J. F. B.: Causes of twentieth-century
539 temperature change near the Earth's surface, *Nature*, 399, 569-572, 10.1038/21164, 1999
- 540 Tie, X. X., Wu, D., and Brasseur, G.: Lung cancer mortality and exposure to atmospheric aerosol particles
541 in Guangzhou, China, *Atmos Environ*, 43, 2375-2377, 10.1016/j.atmosenv.2009.01.036, 2009.
- 542 Wang, H. J., Chen, H. P., and Liu, J. P.: Arctic sea ice decline intensified haze pollution in eastern China, *Atmos*
543 *Oceanic Sci Lett*, 8, 1-9, 10.3878/AOSL20140081, 2015.
- 544 Wang, H. J., and Chen, H. P.: Understanding the recent trend of haze pollution in eastern China: roles of climate
545 change, *Atmos Chem Phys*, 16, 4205-4211, 10.5194/acp-16-4205-2016, 2016.
- 546 Wang, H. J.: On assessing haze attribution and control measures in China, *Atmos Oceanic Sci Lett*, 11, 120-122,
547 10.1080/16742834.2018.1409067, 2018.
- 548 Wang, J., He, J. H., Liu, X. F., and Wu, B. G.: Interannual variability of the Meiyu onset over Yangtze-Huaihe
549 River Valley and analyses of its previous strong influence signal, *Chin Sci Bull*, 54, 687-695,
550 10.1007/s11434-008-0534-8, 2009.
- 551 Wang, J., Zhang, X. Y., Cai, Z. Y., Wang, D. Z., and Chen, H.: Meteorological causes of a heavy air pollution
552 process in Tianjin and its prediction analyses, *Environ Sci Technol*, 38, 77-82, 2015 (in Chinese).
- 553 Wang, J., Zhao, Q. H., Zhu, Z. W., Qi, L., Wang, J. X. L., and He, J. H.: Interannual variation in the number and
554 severity of autumnal haze days in the Beijing-Tianjin-Hebei region and associated atmospheric circulation
555 anomalies, *Dyn Atmos Oceans*, 84, 1-9, 10.1016/j.dynatmoce.2018.08.001, 2018.
- 556 Wang, Y. S., Yao, L., Wang, L. L., Liu, Z. R., Ji, D. S., Tang, G. Q., Zhang, J. K., Sun, Y., Hu, B., and Xin, J. Y.:
557 Mechanism for the formation of the January 2013 heavy haze pollution episode over central and eastern China,
558 *Sci China Earth Sci*, 57, 14-25, 10.1007/s11430-013-4773-4, 2014.
- 559 Wang, Z. F., Li, J., Wang, Z., Yang, W. Y., Tang, X., Ge, B. Z., Yan, P. Z., Zhu, L. L., Chen, X. S., Chen, H. S.,
560 Wang, W., Li, J. J., Liu, B., Wang, X. Y., Wang, W., Zhao, Y. L., Lu, N., and Su, D. B.: Modeling study of
561 regional severe hazes over mid-eastern China in January 2013 and its implications on pollution prevention and
562 control, *Sci China Earth Sci*, 57, 3-13, 10.1007/s11430-013-4793-0, 2014.
- 563 Wu, D., Tie, X. X., Li, C. C., Ying, Z. M., Kai-Hon Lau, A., Huang, J., Deng, X. J., and Bi, X. Y.: An extremely
564 low visibility event over the Guangzhou region: A case study, *Atmos Environ*, 39, 6568-6577,
565 10.1016/j.atmosenv.2005.07.061, 2005.
- 566 Wu, G. X., Li, Z. Q., Fu, C. B., Zhang, X. Y., Zhang, R. Y., Zhang, R. H., Zhou, T. J., Li, J. P., Li, J. D., Zhou, D.
567 G., Wu, L., Zhou, L. T., He, B., and Huang, R. H.: Advances in studying interactions between aerosols and
568 monsoon in China, *Sci China Earth Sci*, 59, 1-16, 10.1007/s11430-015-5198-z, 2016.

- 569 Xiao, D., Li, Y., Fan, S. J., Zhang, R. H., Sun, J. R., and Wang, Y.: Plausible influence of Atlantic Ocean SST
570 anomalies on winter haze in China, *Theor Appl Climatol*, 122, 249-257, 10.1007/s00704-014-1297-6, 2015.
- 571 Xu, P., Chen, Y. F., and Ye, X. J.: Haze, air pollution, and health in China, *Lancet*, 382, 2067,
572 10.1016/S0140-6736(13)62693-8, 2013.
- 573 Xu, X., Zhao, T., Liu, F., Gong, S. L., Kristovich, D., Lu, C., Guo, Y., Cheng, X., Wang, Y., and Ding, G.: Climate
574 modulation of the Tibetan Plateau on haze in China, *Atmos Chem Phys*, 16, 1365-1375,
575 10.5194/acp-16-1365-2016, 2016.
- 576 Xu, X. D., Wang, Y. J., Zhao, T. L., Cheng, X. H., Meng, Y. Y., and Ding, G. A.: “Harbor” effect of large
577 topography on haze distribution in eastern China and its climate modulation on decadal variations in haze China ,
578 *Chin Sci Bull*, 60, 1132-1143, 10.1360/N972014-00101, 2015 (in Chinese).
- 579 Yang, Y., Liao, H., and Lou, S. J.: Decadal trend and interannual variation of outflow of aerosols from East Asia:
580 Roles of variations in meteorological parameters and emissions, *Atmos Environ*, 100, 141-153,
581 10.1016/j.atmosenv.2014.11.004, 2015.
- 582 Yang, Y., Liao, H., and Lou, S. J.: Increase in winter haze over eastern China in recent decades: Roles of variations
583 in meteorological parameters and anthropogenic emissions, *J Geophys Res Atmos*, 121, 13,050-013,065,
584 10.1002/2016JD025136, 2016.
- 585 Yang, Y. R., Liu, X. G., Qu, Y., An, J. L., Jiang, R., Zhang, Y. H., Sun, Y. L., Wu, Z. J., Zhang, F., Xu, W. Q., and
586 Ma, Q. X.: Characteristics and formation mechanism of continuous hazes in China: a case study during the
587 autumn of 2014 in the North China Plain, *Atmos Chem Phys*, 15, 8165-8178, 10.5194/acp-15-8165-2015, 2015.
- 588 Yin, Z. C., and Wang, H. J.: Seasonal prediction of winter haze days in the north central North China Plain, *Atmos
589 Chem Phys*, 16, 14843-14852, 10.5194/acp-16-14843-2016, 2016.
- 590 Yin, Z. C., Wang, H. J., and Chen, H. P.: Understanding severe winter haze events in the North China Plain in 2014:
591 roles of climate anomalies, *Atmos Chem Phys*, 17, 1641-1651, 10.5194/acp-17-1641-2017, 2017.
- 592 You, T., Wu, R. G., Huang, G., and Fan, G. Z.: Regional meteorological patterns for heavy pollution events in
593 Beijing, *J Meteor Res*, 31, 597–611, 10.1007/s13351-017-6143-1, 2017.
- 594 You, Y. C., Cheng, X. G., Zhao, T. L., Xu, X. D., Gong, S. L., Zhang, X. Y., Zheng, Y., Che, H. Z., Yu, C., Chang, J.
595 C., Ma, G. X., and Wu, M.: Variations of haze pollution in China modulated by thermal forcing of the Western
596 Pacific Warm Pool, *Atmosphere*, 9, 314, 10.3390/atmos9080314, 2018.
- 597 Zhang, H., Zhao, S. Y., Wang, Z. L., Zhang, X. Y., and Song, L. C.: The updated effective radiative forcing of
598 major anthropogenic aerosols and their effects on global climate at present and in the future, *Int J Climatol*, 36,
599 4029-4044, 10.1002/joc.4613, 2016.
- 600 Zhang, L., Wang, T., Lv, M. Y., and Zhang, Q.: On the severe haze in Beijing during January 2013: Unraveling the
601 effects of meteorological anomalies with WRF-Chem, *Atmos Environ*, 104, 11-21,
602 10.1016/j.atmosenv.2015.01.001, 2015.
- 603 Zhang, R. H., Li, Q., and Zhang, R. N.: Meteorological conditions for the persistent severe fog and haze event over
604 eastern China in January 2013, *Sci China Earth Sci*, 57, 26-35, 10.1007/s11430-013-4774-3, 2014.
- 605 Zhang, Z. Y., Zhang, X., Gong, D. Y., Kim, S. J., Mao, R., and Zhao, X.: Possible influence of atmospheric
606 circulations on winter haze pollution in the Beijing–Tianjin–Hebei region, northern China, *Atmos Chem Phys*,
607 16, 561-571, 10.5194/acp-16-561-2016, 2016.

608 Zhao, S. Y., Zhang, H., and Xie, B.: The effects of El Niño–Southern Oscillation on the winter haze pollution of
609 China, *Atmos Chem Phys*, 18, 1863–1877, 10.5194/acp-18-1863-2018, 2018.

610 Zhu, X. W., Tang, G. Q., Hu, B., Wang, L. L., Xin, J. Y., Zhang, J. K., Liu, Z. R., Münkel, C., and Wang, Y. S.:
611 Regional pollution and its formation mechanism over North China Plain: A case study with ceilometer
612 observations and model simulations, *J Geophys Res Atmos*, 121, 14574-14588, 10.1002/2016JD025730, 2016.

613 Zhu, Z. W., Li, T., and He, J. H.: Out-of-Phase relationship between boreal spring and summer decadal rainfall
614 changes in southern China, *J Climate*, 27, 1083-1099, 10.1175/jcli-d-13-00180.1, 2014.

615 Zhu, Z. W., and Li, T.: A new paradigm for continental U.S. summer rainfall variability: Asia–North America
616 teleconnection, *J Climate*, 29, 7313-7327, 10.1175/jcli-d-16-0137.1, 2016.

617 Zhu, Z. W., and Li, T.: The record-breaking hot summer in 2015 over Hawaii and its physical causes, *J Climate*, 30,
618 4253-4266, 10.1175/JCLI-D-16-0438.1, 2017.

619 Zhu, Z. W.: Breakdown of the relationship between Australian summer rainfall and ENSO caused by tropical
620 Indian Ocean SST warming, *J Climate*, 31, 2321-2336, 10.1175/jcli-d-17-0132.1, 2018.

621 Zhu, Z. W., and Li, T.: Amplified contiguous United States summer rainfall variability induced by East Asian
622 monsoon interdecadal change, *Clim Dyn*, 50, 3523-3536, 10.1007/s00382-017-3821-8, 2018.

623 Zou, Y. F., Wang, Y. H., Zhang, Y. Z., and Koo, J.-H.: Arctic sea ice, Eurasia snow, and extreme winter haze in
624 China, *Sci Adv*, 3, e1602751, 10.1126/sciadv.1602751, 2017.
625
626
627
628
629
630
631
632
633
634
635
636
637
638
639
640
641
642
643
644
645
646
647
648
649

650 Figures Captions

651 **Figure 1.** Topographic map (shaded; m) for the BTH region and the locations of 20 meteorological sites (colored dots). The dots colored
652 red (light red; magenta) represent significant positive temporal correlation coefficients at the 99% (95%; 90%) confidence level between
653 the AHD_{BTH} and AHD for every individual site on the interannual timescale.

654 **Figure 2.** Time series of the raw AHD_{BTH} (black line; days), along with its interdecadal component (blue line; days) and interannual
655 component (red line; days), for the period 1960–2017. The gray horizontal line delineates the average climate value of the raw AHD_{BTH}
656 during 1960–2017.

657 **Figure 3.** The climatological-mean (1960–2017) autumnal (a) Z500 (contours; gpm), UV850 (vectors; $m s^{-1}$) and total cloud (shaded; %),
658 and (b) surface relative humidity (shaded; %) and surface air temperature (contours; $^{\circ}C$). The gray shaded area denotes the Tibetan
659 Plateau, and the blue dashed box delineates the research domain of the BTH region. The letter A represents the center of anticyclonic
660 circulation.

661 **Figure 4.** Regressed patterns of autumnal meteorological parameters onto the interannual component of the AHD_{BTH} , including (a)
662 surface relative humidity (shaded; %), (b) surface air temperature (shaded; $^{\circ}C$), (c) surface wind speed (shaded; $m s^{-1}$), (d) SLP (shaded;
663 hPa), (e) PBLH (shaded; m), and (f) 500-hPa omega (shaded; $10^{-2} Pa s^{-1}$). Regression coefficients that are significant at the 90%
664 confidence level are stippled. The blue dashed box outlines the research domain of the BTH region.

665 **Figure 5.** Regressed anomalies of autumnal (a) 200-hPa geopotential height (Z200; shaded; gpm) and 200-hPa winds (UV200; vectors; m
666 s^{-1}), (b) Z500 (shaded; gpm) and 500-hPa winds (UV500; vectors; $m s^{-1}$), (c) SST (shaded; $^{\circ}C$) and UV850 (vectors; $m s^{-1}$), (d) SLP
667 (shaded; hPa) and surface winds (vectors; $m s^{-1}$), and (e) precipitation (shaded; $mm day^{-1}$), with respect to the interannual component of
668 the AHD_{BTH} . Regression coefficients that are significant at the 95% (90%) confidence level are stippled (cross hatched). In panels (a) and
669 (b), only the wind vectors with statistical significance above the 90% confidence level are shown. In panel (c), the two red dashed
670 rectangles, labelled R1 and R2, are the key regions where SSTAs are significantly correlated with the interannual component of the
671 AHD_{BTH} ; vectors with scales less than $0.05 m s^{-1}$ are omitted. In panel (d), vectors with scales less than $0.03 m s^{-1}$ are omitted. The blue
672 dashed box delineates the research domain of the BTH region. The letters A and C represent the centers of anticyclonic and cyclonic
673 anomalies, respectively.

674 **Figure 6.** Time series of the normalized interannual component of the AHD_{BTH} (black line), along with the simultaneous SST over R1
675 (red line) and R2 (blue line) for the period 1960–2017. The horizontal dashed lines denote 0.8 of the standard deviation. The numerals
676 labelled at the bottom represent the correlation coefficients (r) between the AHD_{BTH} and simultaneous SST over R1 and R2, separately.
677 The upper and lower dots in the red line indicate the three highest and lowest years of SST over R1, respectively.

678 **Figure 7.** Regressed anomalies of autumnal UV850 (vectors; $m s^{-1}$) with respect to the simultaneous interannual component of the SST
679 over R1. Green arrows represent the wind vectors with statistical significance above the 90% confidence level. The red dashed rectangle
680 labelled R1 is the key region where SSTAs are significantly correlated with the interannual component of the AHD_{BTH} . The blue dashed
681 box delineates the research domain of the BTH region. The gray shaded area denotes the Tibetan Plateau. The letters A and C represent
682 the centers of anticyclonic and cyclonic anomalies, respectively.

683 **Figure 8.** The autumnal composite differences of (a) 200-hPa and (b) 500-hPa WAF (vectors; $m^2 s^{-2}$), geopotential height (contours;
684 gpm), and relative vorticity (shaded; $10^{-5} s^{-1}$) between the three highest and three lowest years of simultaneous SST over R1 (highest
685 minus lowest), as shown in Fig. 6. The red dashed rectangle labelled R1 is the key region where SSTAs are significantly correlated with
686 the interannual component of the AHD_{BTH} . The blue dashed box delineates the research domain of the BTH region.

687 **Figure 9.** Regressed anomalies of autumnal (a) UV850 (vectors; $m s^{-1}$) and SST (shaded; $^{\circ}C$), and (b) precipitation (shaded; $mm day^{-1}$)
688 with respect to the simultaneous interannual component of the SST over R2. In panel (a), green arrows represent the wind vectors with
689 statistical significance above the 99% confidence level, and vectors with scales less than $0.05 m s^{-1}$ are omitted. Regression coefficients
690 that are significant at the 99% confidence level are cross hatched. The dashed red rectangle labelled R2 is the key region where SSTAs are
691 significantly correlated with the interannual component of the AHD_{BTH} . The blue dashed box delineates the research domain of the BTH
692 region. The gray shaded area denotes the Tibetan Plateau. The letter A (C) represents the center of anticyclonic (cyclonic) anomaly.

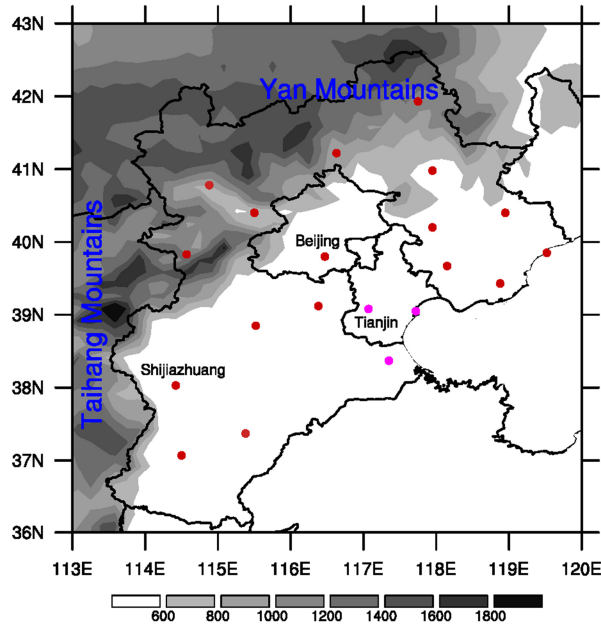
693 **Figure 10.** (a) Latitude–vertical section (112.5° – $130^{\circ}E$) of the autumnal omega (shaded; $10^{-2} Pa s^{-1}$) and (b) longitude–vertical section
694 (35° – $42.5^{\circ}N$) of the autumnal air temperature (shaded; $^{\circ}C$) anomalies regressed onto the simultaneous interannual component of the SST
695 over R2. Regression coefficients that are significant at the 90% confidence level are stippled. The thick blue horizontal bars superimposed
696 onto the abscissa of panels (a) and (b) indicate the latitudes and longitudes of the BTH region, respectively.

697 **Figure 11.** The response of anomalous (a) Z200 (shaded; 10 gpm) and UV200 (vectors; $m s^{-1}$), and (b) Z500 (shaded; 10 gpm) and
698 UV500 (vectors; $m s^{-1}$) in H_NAS . The red contours indicate the imposed idealized heating. The blue dashed box delineates the research
699 domain of the BTH region. The letters A and C represent the centers of anticyclonic and cyclonic anomalies, respectively.

700 **Figure 12.** The response of Z850 (shaded; 10 gpm) and UV850 (vectors; $m s^{-1}$) in H_WNP . The magenta contours indicate the imposed
701 idealized heating. The blue dashed box delineates the research domain of the BTH region. The gray shaded area denotes the Tibetan
702 Plateau. The letter A (C) represents the center of anticyclonic (cyclonic) anomaly.

703 **Figure 13.** Schematic diagram encapsulating the SSTA-induced (warming in R1 and R2) physical mechanisms and pathways connected
704 to above-normal AHD_{BTH} years on the interannual timescale. Anomalous quasi-barotropic anticyclones (A) and cyclones (C) are indicated
705 by blue and red elliptical cycles with arrows separately, denoting large-scale Rossby wave train triggered by the heating to the north of R1.
706 Green arrows depict the key horizontal low-level (850-hPa) airflows. The red, azure and green arrows together exhibit the vertical
707 overturning circulation tied to the SST warming in R2. The left-hand (right-hand) side of the cloud-resembled pattern with violet short
708 dashed lines presents the significant anomalous precipitation induced by SSTAs over R1 (R2). The blue dashed box delineates the
709 research domain of the BTH region.

710



711

712 **Figure 1.** Topographic map (shaded; m) for the BTH region and the locations of 20 meteorological sites (colored dots). The dots colored
 713 red (light red; magenta) represent significant positive temporal correlation coefficients at the 99% (95%; 90%) confidence level between
 714 the AHD_{BTH} and AHD for every individual site on the interannual timescale.

715

716

717

718

719

720

721

722

723

724

725

726

727

728

729

730

731

732

733

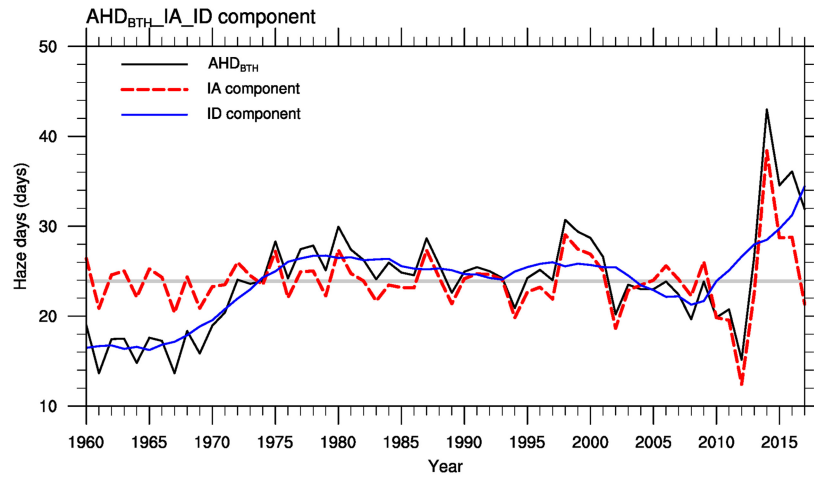
734

735

736

737

738



739

740 **Figure 2.** Time series of the raw AHD_{BTH} (black line; days), along with its interdecadal component (blue line; days) and interannual
 741 component (red line; days), for the period 1960–2017. The gray horizontal line delineates the average climate value of the raw AHD_{BTH}
 742 during 1960–2017.

743

744

745

746

747

748

749

750

751

752

753

754

755

756

757

758

759

760

761

762

763

764

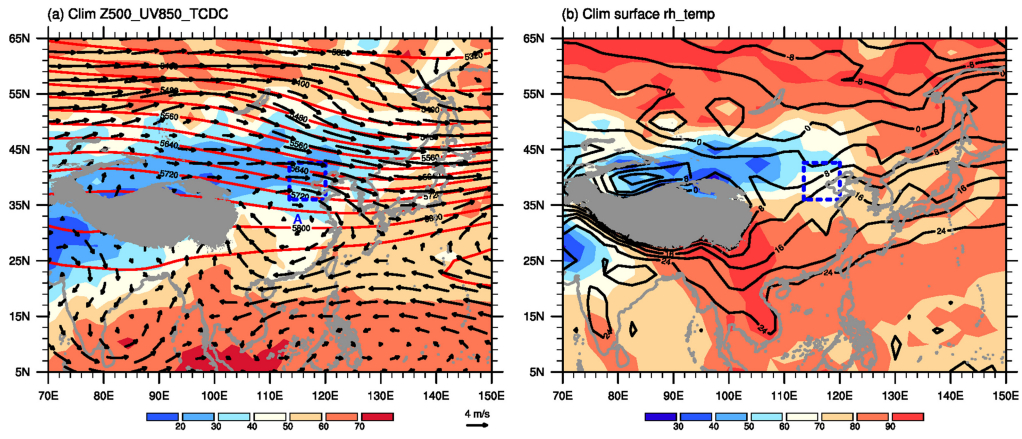
765

766

767

768

769



770

771 **Figure 3.** The climatological-mean (1960–2017) autumnal (a) Z500 (contours; gpm), UV850 (vectors; m s⁻¹) and total cloud (shaded; %),
 772 and (b) surface relative humidity (shaded; %) and surface air temperature (contours; °C). The gray shaded area denotes the Tibetan
 773 Plateau, and the blue dashed box delineates the research domain of the BTH region. The letter A represents the center of anticyclonic
 774 circulation.

775

776

777

778

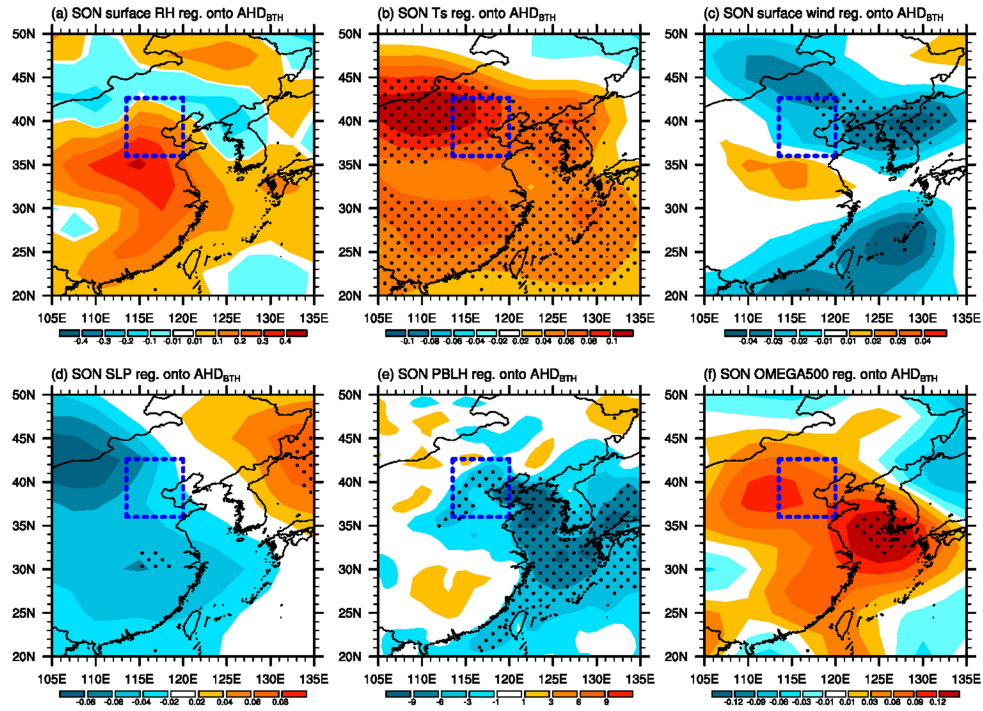
779

780

781

782

783



784

785 **Figure 4.** Regressed patterns of autumnal meteorological parameters onto the interannual component of the AHD_{BTH} , including (a)
 786 surface relative humidity (shaded; %), (b) surface air temperature (shaded; $^{\circ}C$), (c) surface wind speed (shaded; $m s^{-1}$), (d) SLP (shaded;
 787 hPa), (e) PBLH (shaded; m), and (f) 500-hPa omega (shaded; $10^{-2} Pa s^{-1}$). Regression coefficients that are significant at the 90%
 788 confidence level are stippled. The blue dashed box outlines the research domain of the BTH region.

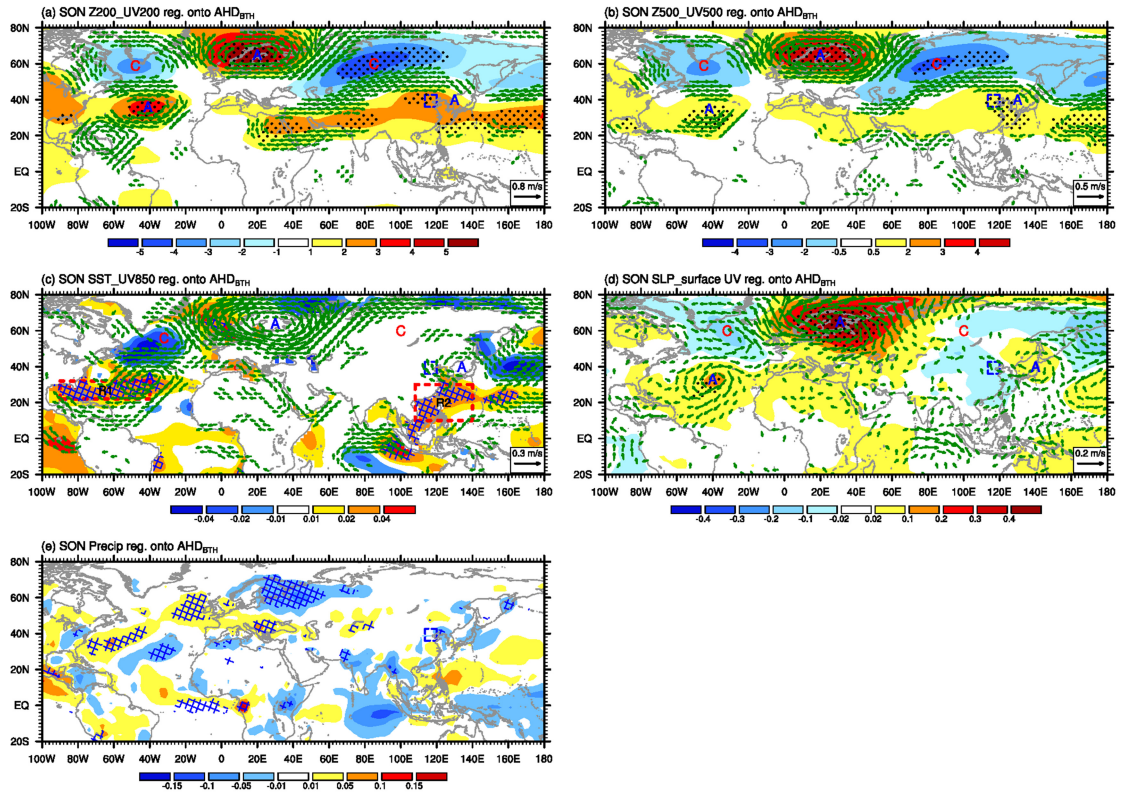
789

790

791

792

793



794

795 **Figure 5.** Regressed anomalies of autumnal (a) 200-hPa geopotential height (Z200; shaded; gpm) and 200-hPa winds (UV200; vectors; $m s^{-1}$), (b) Z500 (shaded; gpm) and 500-hPa winds (UV500; vectors; $m s^{-1}$), (c) SST (shaded; $^{\circ}C$) and UV850 (vectors; $m s^{-1}$), (d) SLP (shaded; hPa) and surface winds (vectors; $m s^{-1}$), and (e) precipitation (shaded; $mm day^{-1}$), with respect to the interannual component of the AHD_{BTH} . Regression coefficients that are significant at the 95% (90%) confidence level are stippled (cross hatched). In panels (a) and (b), only the wind vectors with statistical significance above the 90% confidence level are shown. In panel (c), the two red dashed rectangles, labelled R1 and R2, are the key regions where SSTAs are significantly correlated with the interannual component of the AHD_{BTH} ; vectors with scales less than $0.05 m s^{-1}$ are omitted. In panel (d), vectors with scales less than $0.03 m s^{-1}$ are omitted. The blue dashed box delineates the research domain of the BTH region. The letters A and C represent the centers of anticyclonic and cyclonic anomalies, respectively.

804

805

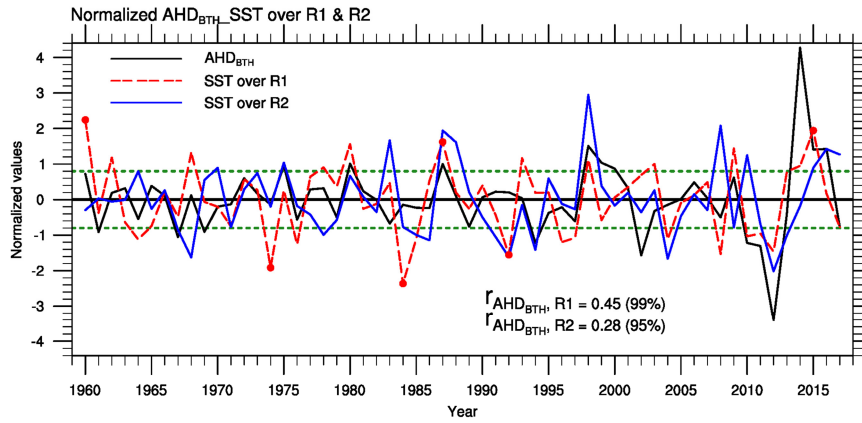
806

807

808

809

810



811

812 **Figure 6.** Time series of the normalized interannual component of the AHD_{BTH} (black line), along with the simultaneous SST over R1
 813 (red line) and R2 (blue line) for the period 1960–2017. The horizontal dashed lines denote 0.8 of the standard deviation. The numerals
 814 labelled at the bottom represent the correlation coefficients (*r*) between the AHD_{BTH} and simultaneous SST over R1 and R2, separately.
 815 The upper and lower dots in the red line indicate the three highest and lowest years of SST over R1, respectively.

816

817

818

819

820

821

822

823

824

825

826

827

828

829

830

831

832

833

834

835

836

837

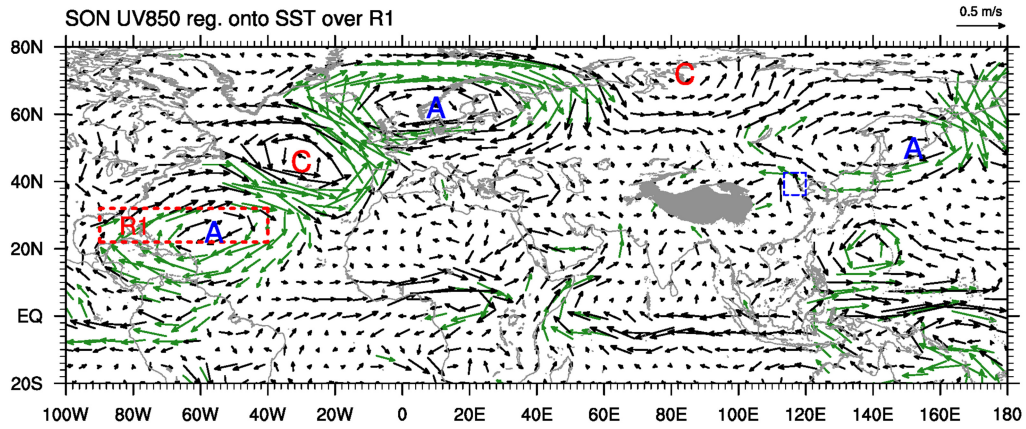
838

839

840

841

842



843

844 **Figure 7.** Regressed anomalies of autumnal UV850 (vectors; m s^{-1}) with respect to the simultaneous interannual component of the SST
 845 over R1. Green arrows represent the wind vectors with statistical significance above the 90% confidence level. The red dashed rectangle
 846 labelled R1 is the key region where SSTAs are significantly correlated with the interannual component of the AHD_{BTH} . The blue dashed
 847 box delineates the research domain of the BTH region. The gray shaded area denotes the Tibetan Plateau. The letters A and C represent
 848 the centers of anticyclonic and cyclonic anomalies, respectively.

849

850

851

852

853

854

855

856

857

858

859

860

861

862

863

864

865

866

867

868

869

870

871

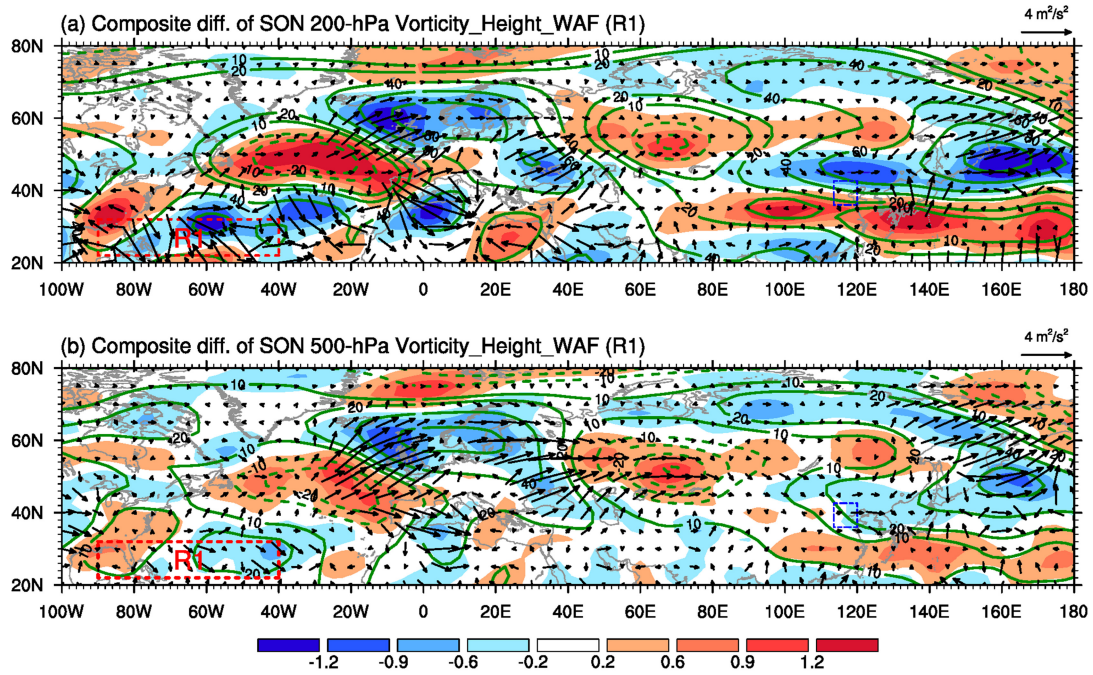
872

873

874

875

876



877

878 **Figure 8.** The autumnal composite differences of (a) 200-hPa and (b) 500-hPa WAF (vectors; $\text{m}^2 \text{s}^{-2}$), geopotential height (contours;
 879 gpm), and relative vorticity (shaded; 10^{-5} s^{-1}) between the three highest and three lowest years of simultaneous SST over R1 (highest
 880 minus lowest), as shown in Fig. 6. The red dashed rectangle labelled R1 is the key region where SSTAs are significantly correlated with
 881 the interannual component of the AHD_{BTH} . The blue dashed box delineates the research domain of the BTH region.

882

883

884

885

886

887

888

889

890

891

892

893

894

895

896

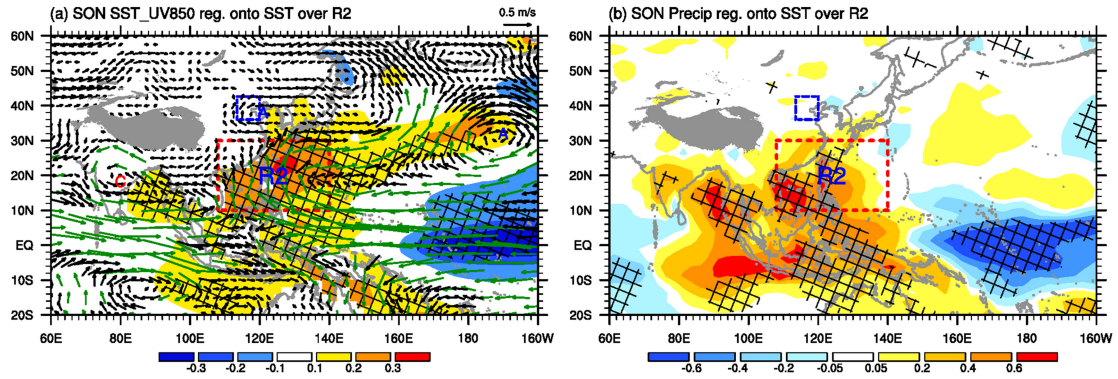
897

898

899

900

901



902

903 **Figure 9.** Regressed anomalies of autumnal (a) UV850 (vectors; m s^{-1}) and SST (shaded; $^{\circ}\text{C}$), and (b) precipitation (shaded; mm day^{-1})
 904 with respect to the simultaneous interannual component of the SST over R2. In panel (a), green arrows represent the wind vectors with
 905 statistical significance above the 99% confidence level, and vectors with scales less than 0.05 m s^{-1} are omitted. Regression coefficients
 906 that are significant at the 99% confidence level are cross hatched. The dashed red rectangle labelled R2 is the key region where SSTAs are
 907 significantly correlated with the interannual component of the AHD_{BTH} . The blue dashed box delineates the research domain of the BTH
 908 region. The gray shaded area denotes the Tibetan Plateau. The letter A (C) represents the center of anticyclonic (cyclonic) anomaly.
 909

910

911

912

913

914

915

916

917

918

919

920

921

922

923

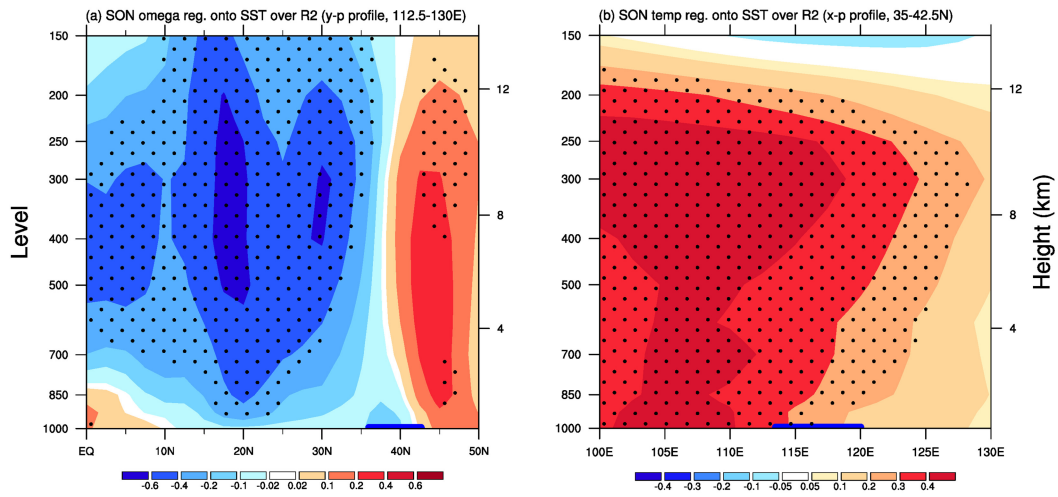
924

925

926

927

928



929

930 **Figure 10.** (a) Latitude–vertical section (112.5°–130°E) of the autumnal omega (shaded; $10^{-2} \text{ Pa s}^{-1}$) and (b) longitude–vertical section
 931 (35°–42.5°N) of the autumnal air temperature (shaded; °C) anomalies regressed onto the simultaneous interannual component of the SST
 932 over R2. Regression coefficients that are significant at the 90% confidence level are stippled. The thick blue horizontal bars superimposed
 933 onto the abscissa of panels (a) and (b) indicate the latitudes and longitudes of the BTH region, respectively.

934

935

936

937

938

939

940

941

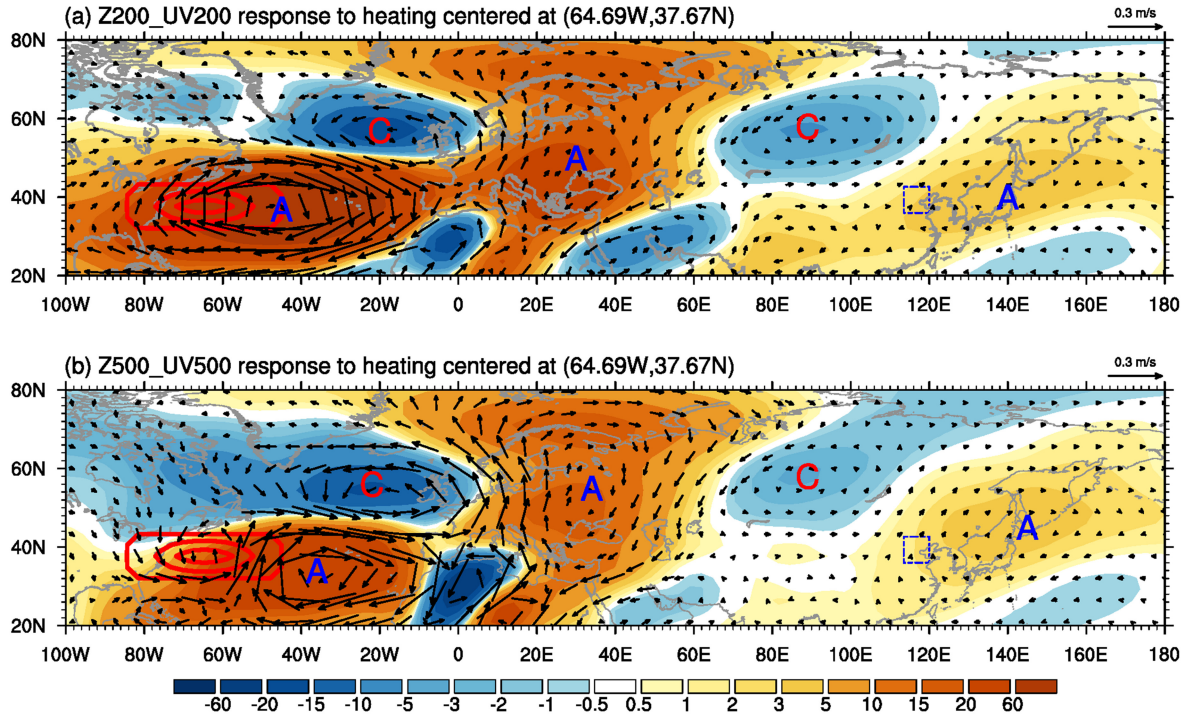
942

943

944

945

946



947

948 **Figure 11.** The response of anomalous (a) Z200 (shaded; 10 gpm) and UV200 (vectors; $m s^{-1}$), and (b) Z500 (shaded; 10 gpm) and
 949 UV500 (vectors; $m s^{-1}$) in H_NAS. The red contours indicate the imposed idealized heating. The blue dashed box delineates the research
 950 domain of the BTH region. The letters A and C represent the centers of anticyclonic and cyclonic anomalies, respectively.

951

952

953

954

955

956

957

958

959

960

961

962

963

964

965

966

967

968

969

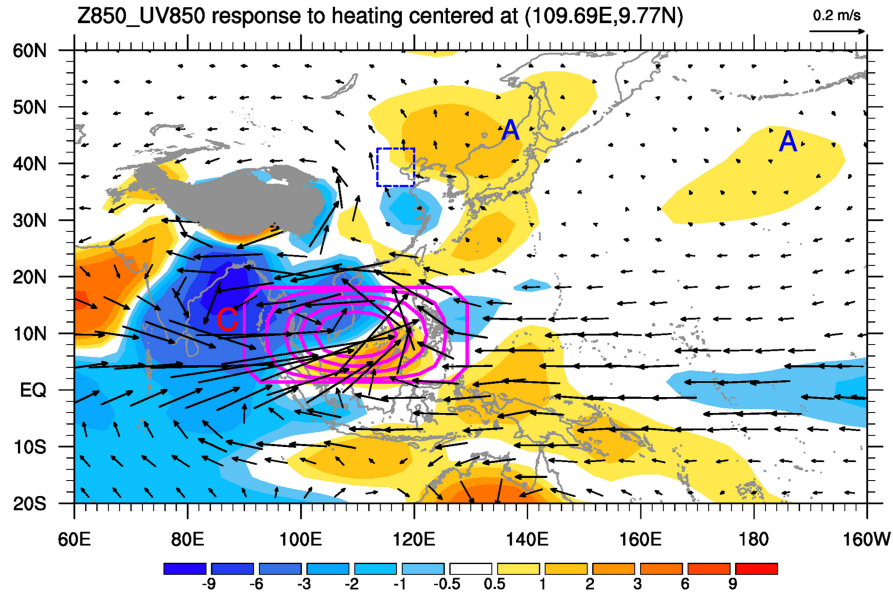
970

971

972

973

974



975

976 **Figure 12.** The response of Z850 (shaded; 10 gpm) and UV850 (vectors; $m s^{-1}$) in H_WNP. The magenta contours indicate the imposed
 977 idealized heating. The blue dashed box delineates the research domain of the BTH region. The gray shaded area denotes the Tibetan
 978 Plateau. The letter A (C) represents the center of anticyclonic (cyclonic) anomaly.

979

980

981

982

983

984

985

986

987

988

989

990

991

992

993

994

995

996

997

998

999

1000

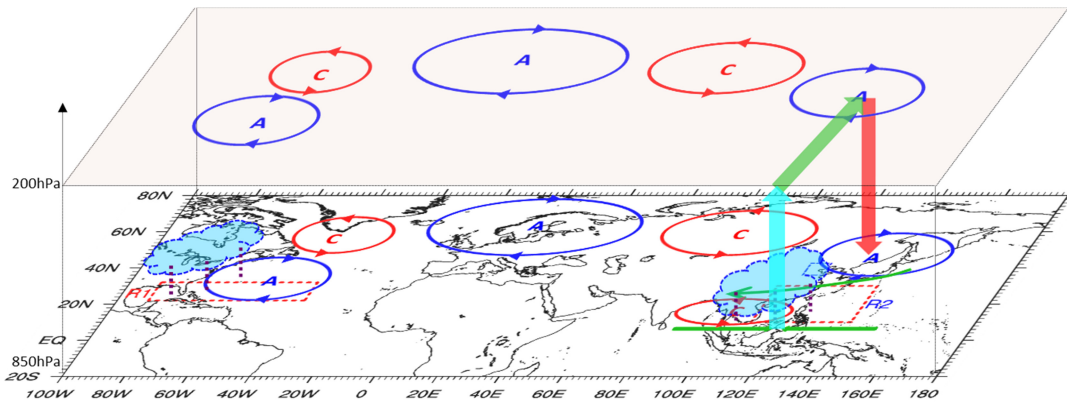
1001

1002

1003

1004

1005



1006

1007 **Figure 13.** Schematic diagram encapsulating the SSTA-induced (warming in R1 and R2) physical mechanisms and pathways connected
 1008 to above-normal AHD_{BTH} years on the interannual timescale. Anomalous quasi-barotropic anticyclones (A) and cyclones (C) are indicated
 1009 by blue and red elliptical cycles with arrows separately, denoting large-scale Rossby wave train triggered by the heating to the north of R1.
 1010 Green arrows depict the key horizontal low-level (850-hPa) airflows. The red, azure and green arrows together exhibit the vertical
 1011 overturning circulation tied to the SST warming in R2. The left-hand (right-hand) side of the cloud-resembled pattern with violet short
 1012 dashed lines presents the significant anomalous precipitation induced by SSTAs over R1 (R2). The blue dashed box delineates the
 1013 research domain of the BTH region.

1014

1015

1016

1017

1018

1019

1020

1021

1022

1023

1024

1025

1026

1027

1028

1029

1030

1031

1032

1033

1034

1035

1036

1037

1038

1039

1040